



Photoacoustic imaging of elevated glutathione in models of lung cancer for companion diagnostic applications

Melissa Y. Lucero and Jefferson Chan  

Companion diagnostics (CDx) are powerful tests that can provide physicians with crucial biomarker information that can improve treatment outcomes by matching therapies to patients. Here, we report a photoacoustic imaging-based CDx (PACDx) for the selective detection of elevated glutathione (GSH) in a lung cancer model. GSH is abundant in most cells, so we adopted a physical organic chemistry approach to precisely tune the reactivity to distinguish between normal and pathological states. To evaluate the efficacy of PACDx in vivo, we designed a blind study where photoacoustic imaging was used to identify mice bearing lung xenografts. We also employed PACDx in orthotopic lung cancer and liver metastasis models to image GSH. In addition, we designed a matching prodrug, PARx, that uses the same S_NAr chemistry to release a chemotherapeutic with an integrated PA readout. Studies demonstrate that PARx can inhibit tumour growth without off-target toxicity in a lung cancer xenograft model.

Despite progress in the diagnosis, treatment and management of cancer, nearly 10 million individuals will die each year, with lung cancer being the leading cause¹. An emerging technology that can potentially improve these statistics is companion diagnostics (CDx)²—tests that provide essential information for determining which patients may benefit from a particular treatment by detecting biomarkers that are critical for drug activation³. Current US Food and Drug Administration (FDA)-approved CDx are designed for in vitro testing and thus cannot account for variations in the tumour microenvironment that can impact drug efficacy. To provide accurate, real-time information, it is crucial to develop new molecular imaging-based CDx, as well as corresponding drugs for aberrant cancer properties. However, most clinically approved imaging agents for cancer target cell surface biomarkers through stoichiometric binding events. In addition to poor signal-to-noise, binding-based strategies preclude the detection of small-molecule targets, such as glutathione (GSH). Activity-based sensing (ABS) is a powerful alternative that relies on the selective detection of chemical reactivity. In contrast to fluorescence-based ABS probes, which can only operate in the millimetre depth range due to scattering and light attenuation, the corresponding chemical tools for photoacoustic (PA) imaging can be employed as a CDx for in vivo testing. PA is a non-invasive modality that commonly utilizes near-infrared (NIR) light to induce the generation of an ultrasound signal. Because clinically relevant ultrasound frequencies travel through biological tissues with minimal perturbation, it is possible to pinpoint the source of the signal to achieve high-resolution images (tens of micrometres) in the centimetre range⁴. Label-free PA imaging has already been employed clinically for the detection of breast cancer⁵, thyroid cancer⁶, inflammatory arthritis⁷ and scleroderma⁸. Recently, our group and others have expanded the scope of PA imaging through the development of acoustogenic ABS probes^{9,10}. Select examples include imaging agents for the detection of metal ion dysregulation^{11–15}, hypoxia^{16–20}, proteases^{21,22} and signalling molecules (for example, nitric oxide^{23–25} and hydrogen sulfide²⁶). In this Article, we leverage classic principles in physical organic chemistry to guide the

development of the first PA imaging-based CDx (PACDx), as well as a matching gemcitabine-based prodrug (PARx). Application of PACDx and PARx in an unprecedented blind study allowed us to successfully identify and treat mice with lung cancer, respectively. Additionally, our new CDx was employed in orthotopic lung cancer and liver metastasis models to demonstrate its broad utility. This application is important, because it overcomes an outstanding challenge in the field of PA imaging, which is to detect biomarkers in the lung region.

Results

Physical organic approach to guide the design of PACDx. GSH is an abundant biological thiol that is essential for maintaining redox homeostasis and detoxifying xenobiotics²⁷. Aberrant changes in the cellular levels of GSH are correlated with a variety of pathologies, such as cancer²⁸. Among the various cancer types, non-small cell lung carcinoma has the largest change in GSH levels in both patient-derived tissue samples (up to fourfold)²⁹ and human cell lines (up to sevenfold)^{30,31}, relative to healthy tissue and non-cancerous cell lines, respectively. In this study, we chose to develop a CDx assay for lung cancer based on the detection of GSH via PA imaging. Importantly, even at the onset of cancer, GSH levels are elevated, presenting exciting opportunities for early cancer detection³².

The design of PACDx features two key elements, a PA dye capable of generating a strong PA signal upon irradiation and a trigger for detecting GSH in its reduced form (Fig. 1a). In addition to its large extinction coefficient ($\epsilon = >10^4 \text{ M}^{-1} \text{ cm}^{-1}$) in the near-infrared region, the hemicyanine dye (HD) platform was selected because of its lipophilic cationic character, which can enhance uptake by tumour cells and render the resultant probe a poor substrate for glutathione S-transferase (GST), an abundant cytosolic enzyme that catalyses the conjugation of GSH to electrophilic centres^{33,34}. We deemed this to be important, because the expression of GST may vary in cancer and, therefore, cross-reactivity can confound the imaging results. We employed a physical organic approach to

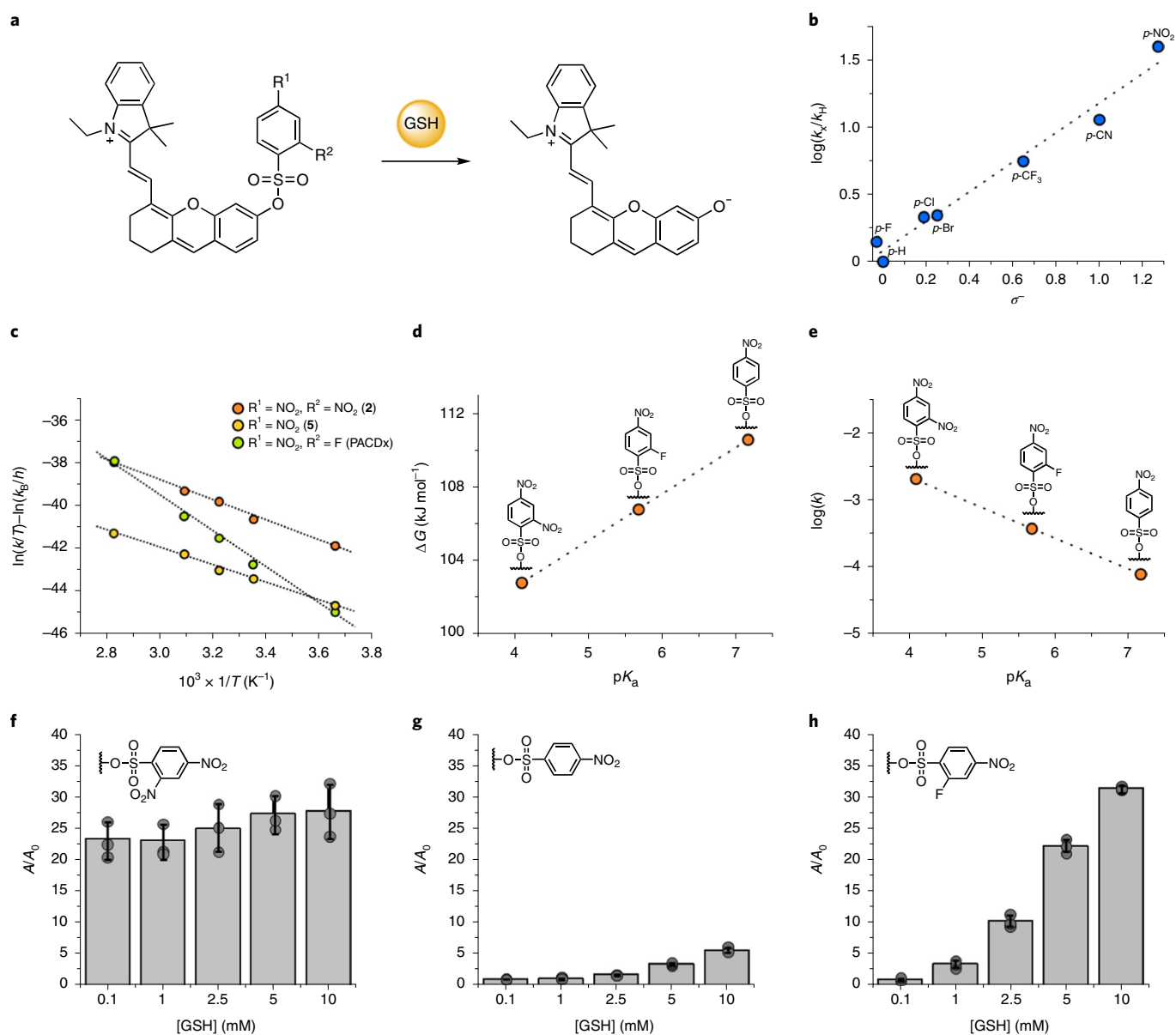


Fig. 1 | Application of physical organic chemistry to tune S_NAr reactivity for GSH sensing. **a**, General schematic for GSH-responsive photoacoustic companion diagnostics. **b**, Hammett plot for the S_NAr reaction between *para*-substituted benzenesulfonyls and 10 mM GSH at 120 °C. The dotted line is the best linear fit of the rate constant data. k_X and k_H are rate constants for when the *para*-substituent is X or H, respectively. **c**, Eyring plots for **2**, **5** and PACDx reacting with GSH (structures of **2**, **5** and PACDx are shown as insets in **f–h**). The dotted lines represent the best linear fits. k , rate constant; T , temperature; k_B , Boltzmann constant; h , Planck's constant. **d,e**, Brønsted plots indicating the linear relationship between ΔG (**d**) and $\log(k)$ (**e**) and pK_a ($R^2=1.0$ and 0.99 , respectively) for **2**, **5** and PACDx reacting with GSH at 37 °C. **f–h**, Dose-dependent activation of **2** (**f**), **5** (**g**) and PACDx, with [GSH] of 0.1–10 mM (**h**). A and A_0 are defined as the final and initial absorbance values, respectively. All assays were performed at pH 7.4, 70% PBS/MeCN. Data are presented as mean values \pm s.d. ($n=3$ independent experiments).

develop a precision-tuned, GSH-responsive trigger that can distinguish GSH levels between lesions and healthy tissue. This represents a substantial challenge, because existing triggers based on disulfide exchange³⁵ and S_NAr ³⁶ chemistry are too reactive. For example, installation of the common 2,4-dinitrobenzenesulfonate trigger onto our PA platform afforded a probe that could not distinguish GSH levels across several mammalian cell lines (Supplementary Fig. 1), because it was fully activated by only 100 μ M GSH within several minutes (\sim 10-fold less than physiological levels; Fig. 1f). To establish a structure–reactivity relationship, we synthesized a panel of nine probes featuring a range of electron-withdrawing and -donating

groups at the *para* position. The resultant Hammett plot revealed a linear correlation between $\log(k_X/k_H)$ and the corresponding σ^- constants (k_X and k_H are rate constants for when the *para*-substituent is X or H, respectively; σ^- is the substituent constant) (Fig. 1b)³⁷. A positive ρ value of 1.10 indicates that electron-deficient substituents at this position were more efficient at stabilizing the Meisenheimer complex, resulting in enhanced reactivity (ρ is the reaction constant). Unfortunately, the most reactive probe in this series (*p*-nitro) was only partially activated, to give a 5.6-fold turn-on response after treatment with 10 mM GSH for 1 h (Fig. 1g). However, a dose- and time-dependent response was evident. Encouraged by these results,

we synthesized an additional four probes with both *ortho*- and *para*-electron-withdrawing groups to further increase the S_NAr reactivity (Supplementary Fig. 2). As anticipated from our structure–reactivity data, installation of a fluoro substituent at the *ortho* position resulted in a highly optimized trigger (Fig. 1b). Activation of the resulting probe, PACDx, under physiological conditions was completely attenuated. On the other hand, a dose-dependent signal increase of up to 31.6-fold was observed when PACDx was incubated with 10 mM GSH for 1 h. Rate constants for the S_NAr reaction for PACDx, the *p*-nitro analogue and the 2,4-dinitro congener were measured at various temperatures to construct the corresponding Eyring plots (Fig. 1c). The derived activation parameters for PACDx are $\Delta H^\ddagger = 70.5 \text{ kJ mol}^{-1}$ and $\Delta S^\ddagger = -117.1 \text{ J mol}^{-1} \text{ K}^{-1}$. These data suggest that the S_NAr reaction involves a highly ordered transition state, which probably results from effective stabilization of the Meisenheimer complex. The Gibbs free energy of activation (ΔG^\ddagger) for PACDx was calculated to be $106.8 \text{ kJ mol}^{-1}$, which indicates that the S_NAr reaction was energetically more favourable than the *p*-nitro analogue, but less favourable compared to the 2,4-dinitro congener. Finally, we constructed two Brønsted relationship graphs where the pK_a values of the corresponding phenols were plotted against ΔG^\ddagger (Fig. 1d) and $\log(k)$ (Fig. 1e). In both cases, we observed a linear correlation with R^2 values of 1.00, suggesting that this information can guide probe design involving S_NAr chemistry. All pertinent results are summarized in Supplementary Table 1.

Evaluation of PACDx in vitro and in live cells. Before activation, PACDx does not absorb strongly within the PA window (680–950 nm). However, treatment with GSH induces a bathochromic shift (Fig. 2a). Irradiation at λ_{max} (690 nm) yields the strongest PA response in vitro (Fig. 2b). A dose-dependent signal enhancement with a limit of detection of 0.39 mM was observed when PACDx was treated with GSH (Fig. 2c,d). By contrast, there was no notable reactivity when the probe was incubated with cysteine (200 μM) or homocysteine (100 μM) (Supplementary Fig. 5). Next, we evaluated the performance of PACDx in A549 lung cancer cells, U87 glioblastoma cells and HEK 293 cells (a non-cancerous cell line) using confocal microscopy. PACDx was highly fluorescent in A549 cells, with a cytosolic and mitochondrial staining pattern (Fig. 2e). However, when cells were pretreated with *N*-ethylmaleimide, a reagent used to reduce the levels of intracellular thiols, the fluorescence signal was attenuated by ~50% (Fig. 2f). To confirm that the decrease in intensity was due to GSH depletion, a third set of cells were treated with a non-responsive control probe (Ctrl-PACDx, Supplementary Fig. 6 and Fig. 2g,h). A trend comparable to that for A549 cell imaging was observed in U87 cells (Supplementary Fig. 7). When A549 and U87 cells were pretreated with ethacrynic acid³⁸, a potent reversible inhibitor of human GST, no effect on probe activation was observed, which suggests that activation of PACDx is independent of GST enzymatic activity (Supplementary Fig. 8).

For PACDx to function as an effective CDx, it is essential for it to be able to accurately differentiate the relative GSH levels in lung cancer cells compared to healthy cells. The intensity of PACDx in A549 cells was indeed the highest relative to U87 and HEK 293 cells (Fig. 2i). However, it is important to note that the signal from the U87 cells was notably lower than that of the HEK 293 cells. To account for possible variations in probe uptake and retention, we incubated PACDx with cell lysates and obtained consistent results (Supplementary Fig. 9). This suggests that the intracellular levels of GSH are highest in A549 cells and lowest in U87 cells. This was confirmed with the established Ellman's assay, which allows for accurate quantification of GSH levels in cell lysates (Fig. 2j)³⁹.

Design and synthesis of PARx. Next, we turned our attention to designing a prodrug invoking the same GSH-mediated chemistry. We rationalized it would be possible to append a chemotherapeutic

to the PACDx core by strategically installing a hydroxymethyl handle *ortho* to the phenolic alcohol. On removal of the trigger, the resultant phenolate intermediate can fragment via a 1,4-elimination pathway to release the drug and the corresponding dye (HD-CH₂OH) for PA imaging (Fig. 3a). We chose to append gemcitabine, an FDA-approved drug, because it is commonly used to treat non-small cell lung cancer through the inhibition of DNA synthesis^{40,41}. However, as with many chemotherapeutics, gemcitabine indiscriminately targets any rapidly dividing cell in the body, which results in adverse effects such as severe liver toxicity⁴². Masking the primary alcohol with a variety of capping groups has led to the development of gemcitabine-based prodrugs displaying attenuated cytotoxicity until they are activated⁴³. Although we could have directly modified gemcitabine with our new 2-fluoro-4-nitrobenzenesulfonyl trigger, we wanted to utilize the lipophilic cationic dye for targeting and to leverage the PA imaging capabilities of the resulting prodrug (herein named PARx) to monitor drug release in real time.

PARx was synthesized starting from the sequential reduction of 2,4-dihydroxybenzaldehyde and *tert*-butyl(dimethyl)silyl protection to afford **16** in 61% yield (Supplementary Information). In situ deprotection of the phenolic alcohols with sodium hydride facilitated a nucleophilic substitution and retro-Knoevenagel sequence with Cy7-Cl to obtain **17**. The GSH-responsive trigger was installed, and the primary alcohol was deprotected under acidic conditions to yield **18** (Ctrl-PARx-2) in 46% over two steps. Finally, a chloroformate intermediate was generated using phosgene and then reacted with gemcitabine to obtain PARx (Supplementary Information).

Evaluation of PARx in vitro and in live cells. With PARx in hand, we first confirmed that attaching gemcitabine did not alter the PA imaging properties or the responsiveness of the GSH trigger (Fig. 3b–d and Supplementary Fig. 10). Interestingly, we observed that PARx consistently yielded a more intense PA signal compared to PACDx, presumably due to the larger PA brightness value ($\epsilon \times (1 - \Phi_{\text{fl}})$)¹⁹, where Φ_{fl} is fluorescence quantum yield. We also demonstrated that PARx displayed exceptional selectivity against a panel of metal ions, amino acids, reductants, reactive nitrogen and oxygen species, metabolic liver enzymes and competing thiols (Fig. 3e). Next, we employed MS and NMR analyses to confirm that GSH mediates the release of gemcitabine (Supplementary Figs. 11 and 12). To further support these results, we prepared a control compound (Ctrl-PARx-1) that is equipped with an unreactive 4-methoxybenzenesulfonyl trigger (Supplementary Fig. 13). MS analysis revealed that both the trigger and carbonate linkage of Ctrl-PARx-1 were stable in the presence of 10 mM GSH for at least 1 h (Supplementary Fig. 14). Moreover, PARx could readily distinguish GSH levels in live A549, U87 and HEK 293 cells, independent of GST activity (Fig. 3f and Supplementary Figs. 16 and 17). Finally, we assessed the cytotoxicity of PARx in A549 cells using the MTT assay and observed dose-dependent toxicity that is comparable to free gemcitabine. By contrast, with treatment with either Ctrl-PARx-1 or Ctrl-PARx-2, the cytotoxicity was significantly attenuated (Fig. 3g). MTT assays in U87 cells established that PARx requires the elevated levels of GSH found in A549 cells to effectively mediate gemcitabine release (Supplementary Fig. 18).

In vivo imaging of GSH and tumour inhibition. To evaluate the in vivo efficacy of the PACDx and PARx pair, we established an A549 xenograft model of lung cancer. After the tumours had grown to ~100 mm³, we administered PACDx via intratumoral injection. Irradiation at 680 nm (the optimal in vivo wavelength) 1 h post-injection resulted in a ~1.5-fold PA turn-on response relative to the control flank. Next, we introduced PARx via systemic administration to determine its biodistribution profile, as well as potential off-target cytotoxic effects. We collected tissue from vital organs 1 h post-injection for PA imaging analysis. The average PA signals from

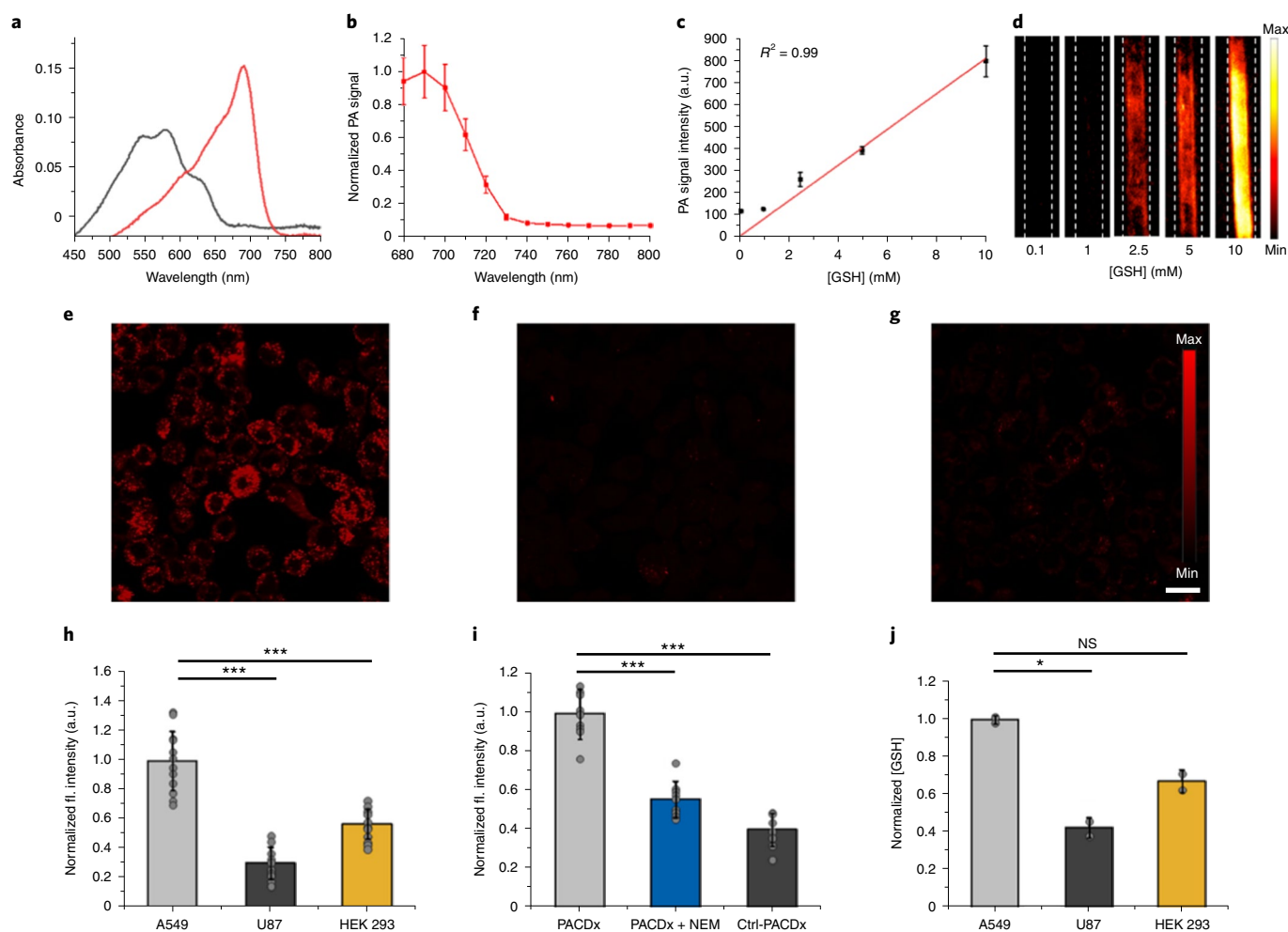


Fig. 2 | Evaluation of PACDx GSH-responsiveness in vitro and in cellulo systems. **a**, Absorbance profile of 5 μ M PACDx before (black line) and after (red line) treatment with 10 mM GSH. **b**, PA spectra of 50 μ M turned-over HD dye. **c,d**, PA signal ($n=3$ independent experiments) (**c**) and PA images of PACDx (**d**) in response to GSH. Samples were irradiated at 690 nm. All in vitro assays were performed at 37 $^{\circ}$ C, pH 7.4, with 70% PBS/MeCN, and data were collected after 1 h. **e-g**, Confocal microscopy image representing A549 cells treated with 5 μ M PACDx for 1 h at 37 $^{\circ}$ C (**e**), A549 cells pretreated with 1 mM *N*-ethylmaleimide (NEM) then incubated with 5 μ M PACDx for 1 h at 37 $^{\circ}$ C (**f**) and A549 cells treated with 5 μ M Ctrl-PACDx for 1 h at 37 $^{\circ}$ C (**g**). Scale bar, 20 μ m. **h**, Normalized fluorescence intensity obtained from cell imaging under the conditions in **e-g**. Data are presented as mean values \pm s.d. ($n=12$ biologically independent samples). **i**, Normalized fluorescence intensity obtained from cell imaging A549, U87 and HEK 293 cells with 5 μ M PACDx for 1 h at 37 $^{\circ}$ C. Data are presented as mean values \pm s.d. ($n=12$ biologically independent samples). **j**, Normalized [GSH] obtained from Ellman's assay. Data are presented as mean values \pm s.d. ($n=2$ biologically independent samples). Statistical analysis was performed using a two-tailed Student's *t*-test ($\alpha=0.05$), *** $P < 0.001$, ** $P < 0.01$, * $P < 0.05$. NS, not significant.

the heart, kidneys, liver and spleen were comparable between the treatment and control groups (Fig. 4a,b). By contrast, the average PA intensity was 1.2-fold higher in the tumour for the PARx-treated animals. This trend suggests selective activation and drug release. Moreover, these results also suggest PARx will not have off-target toxicity. This was confirmed by performing histological staining, which revealed that there was minimal toxicity in all organs examined (Fig. 4c). However, PARx was highly toxic in tumour tissue, as indicated by the decrease in the number of stained nuclei. In addition, terminal deoxynucleotidyl transferase dUTP nick end labelling (TUNEL) staining revealed that PARx-treated tumours experienced significantly greater cell death via apoptosis ($54.3 \pm 7.4\%$) compared to control tumours ($1.9 \pm 1.9\%$) (Fig. 4d,e).

Over a 21-day period, PARx was intratumorally injected into A549 xenografts every seven days. For this initial experiment, we opted for local administration because we wanted to bypass systemic and metabolic processes. PA imaging was performed 1 h after treatment to monitor gemcitabine release (Supplementary Fig. 19).

Compared to control tumours (Fig. 5a,d), the PA signal was higher in PARx-treated tumours. This indicates PARx activation (Fig. 5b,d), leading to complete attenuation of tumour growth (Fig. 5e). By contrast, tumours grew up to ~ 600 mm³ in size when animals received a vehicle control. To evaluate the systemic compatibility of PARx, we retro-orbitally administered PARx every seven days over the course of a 21-day period (Fig. 5e). Of note, PA monitoring was not employed during the treatment period beyond the first imaging session. The inhibition of tumour growth was nearly identical to the results obtained via intratumoral administration. The body weight of each animal was monitored as a measure of general toxicity. Under no treatment conditions did we observe any loss of weight (Fig. 5f) or change in behaviour⁴⁴. To further challenge the selectivity of PARx, we increased the dosing frequency to once every three days (Supplementary Fig. 20). We hypothesized that we would not see any adverse effects, especially in the liver, where severe damage is common with free gemcitabine. Indeed, we did not observe a change in the body weight (Supplementary Fig. 21) or liver damage.

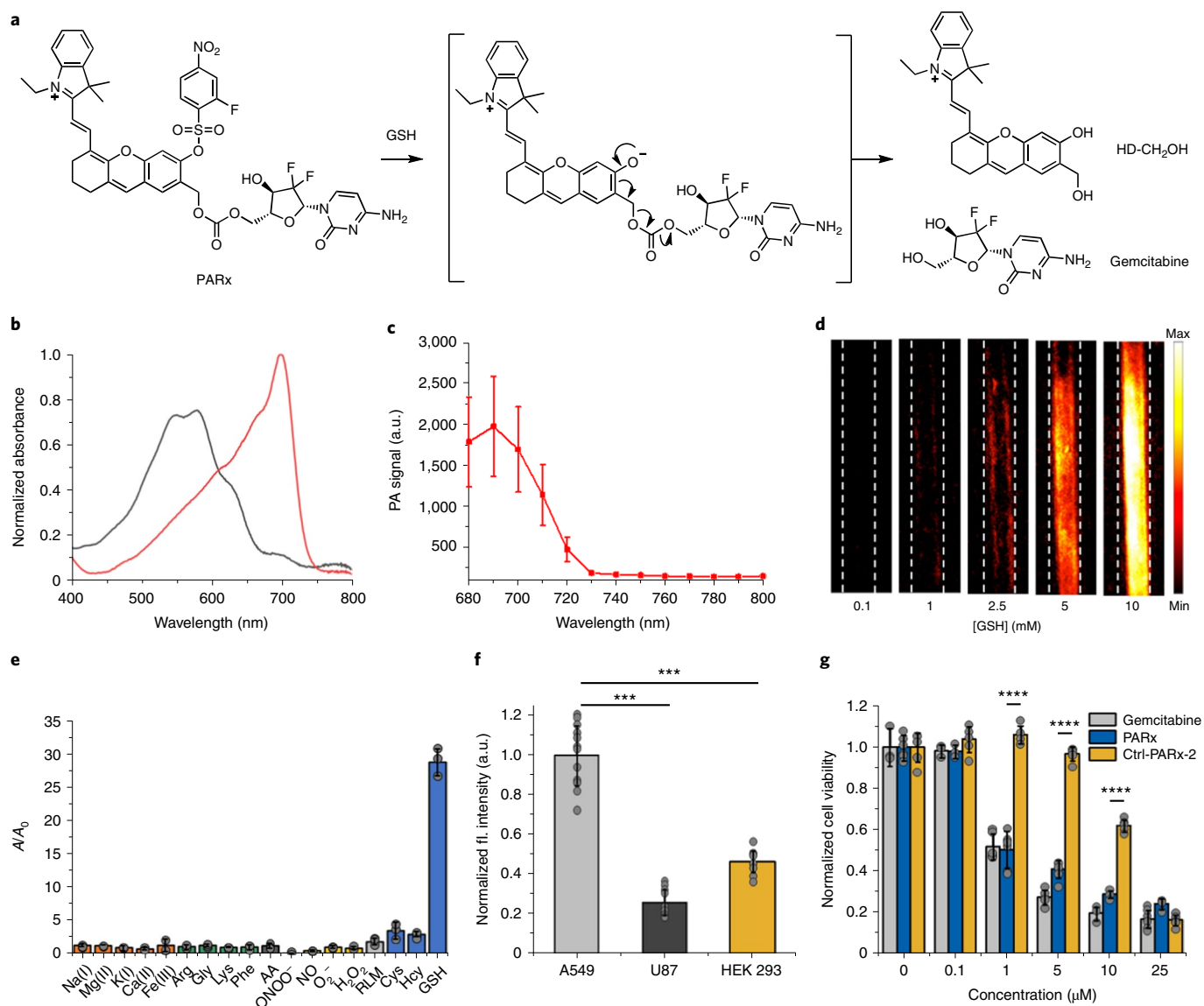


Fig. 3 | Development of PARx, a gemcitabine-based prodrug with matching GSH reactivity. **a**, Reaction scheme of PARx with GSH to release HD-CH₂OH and gemcitabine. **b**, Normalized absorbance profile of 5 μM PARx before (black line) and after (red line) treatment with 10 mM GSH at 37 °C for 1 h (pH 7.4, 70% PBS/MeCN). **c**, PA spectra of 50 μM turned-over HD-CH₂OH dye in 70% PBS/MeCN. **d**, PA images of PARx in response to GSH. Samples were irradiated at 690 nm. **e**, Reactivity of PARx with biologically relevant metals, amino acids, rat liver microsomes (RLM), ascorbic acid (AA), reactive nitrogen species, reactive oxygen species and thiols after incubation for 1 h at 37 °C. **f**, Normalized fluorescence intensity obtained from cell imaging A549, U87 and HEK 293 cells with 5 μM PARx for 1 h at 37 °C. Data are presented as mean values ± s.d. (n = 12 biologically independent samples). Statistical analysis was performed using a two-tailed Student's *t*-test (α = 0.05), ****P* < 0.001, ***P* < 0.01, **P* < 0.05. **g**, Cell viability assay using various concentrations of gemcitabine, PARx and Ctrl-PARx-2 after a 48-h incubation with A549 cells. Data are presented as mean values ± s.d. (n = 6 biologically independent samples). Statistical analysis was performed using a two-way analysis of variance with a Dunnett's multiple comparisons test (α = 0.05); ****adjusted *P* > 0.0001.

Application of PACDx in a blind study. To evaluate the performance of PACDx as a CDx, we designed a blind study to identify animals with lung cancer based on GSH levels. First, a group of nude mice were implanted with either A549 or U87 cells. After the animals were tagged and randomized by a second researcher, their identity was concealed until completion of the study. The purpose of implanting U87 cells, as opposed to no tumours, was to ensure that there would be no biasing of the results based on appearance. Next, we measured the PA intensity change after administration of a vehicle to healthy tissue (1.06 ± 0.17 , $n = 9$) to establish a diagnostic threshold (mean value + 2 s.d.). After the tumours had grown to $\sim 100 \text{ mm}^3$, PACDx was administered to perform PA imaging

(Fig. 6a). We identified one animal that was one s.d. above the mean (1.30) and two animals two s.d. above the mean (1.47 and 1.61) (Fig. 6b). These three subjects (out of seven, total) were categorized to 'group 1', which we assigned to be mice bearing A549 tumours. The remaining four animals (0.84, 1.05, 1.06 and 1.07) were grouped into 'group 2' (Fig. 6b). Although the aim of the study was to demonstrate that PACDx can be used to identify animals that would respond to PARx, we decided to treat both groups with the prodrug. We hypothesized that prodrug treatment of the first group would result in substantial tumour attenuation. Moreover, we predicted that the administration of PARx to the second group would afford no PA signal enhancement due to lower intratumoral

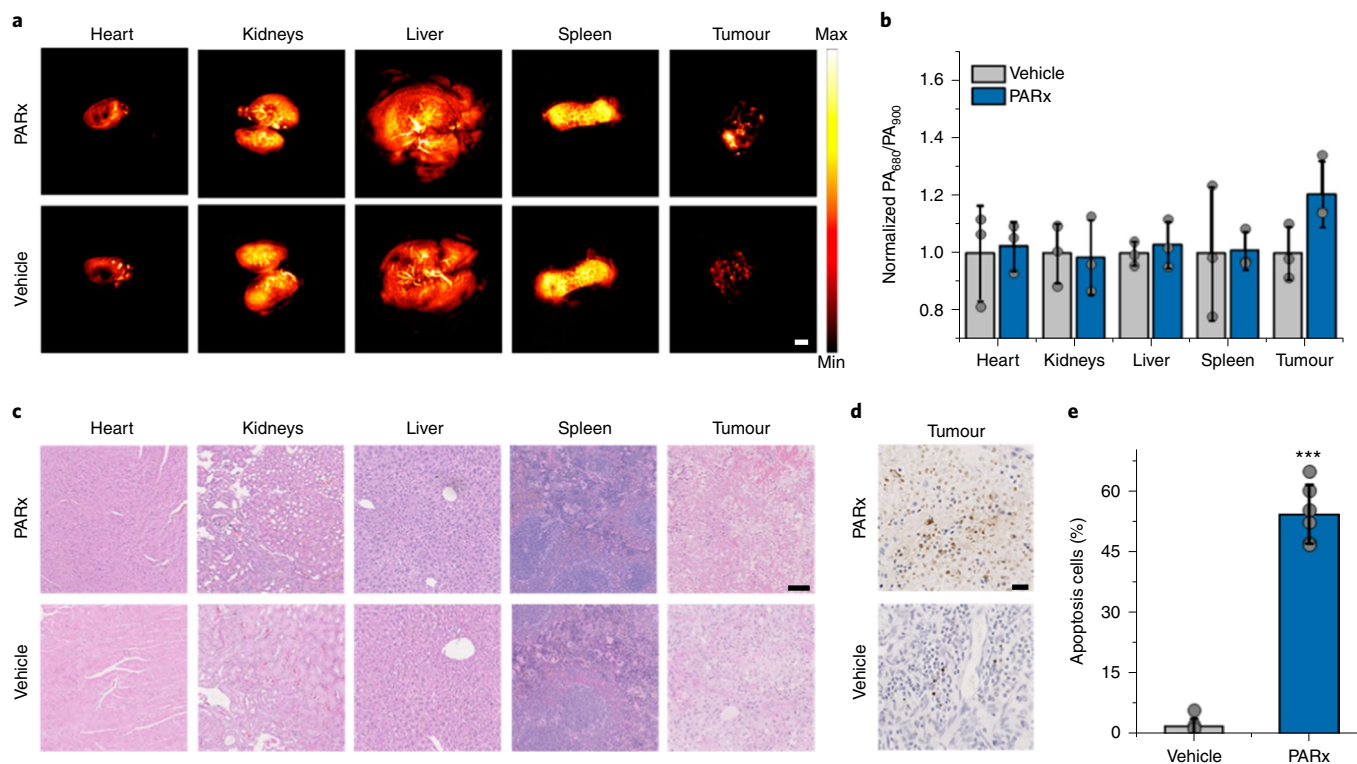


Fig. 4 | Assessment of PARx biodistribution and in vivo activation. **a**, Representative ex vivo PA images of heart, kidneys, liver, spleen and tumour after systemic injection of PARx (400 μ M, 10% dimethyl sulfoxide/phosphate buffered saline (DMSO/PBS), retro-orbital injection) or vehicle. Samples were irradiated at 680 nm. Scale bar, 2 mm. **b**, Normalized PA signal relative to the PA signal at 900 nm (PARx does not absorb at this wavelength) after systemic injection of PARx or vehicle. Data are presented as mean values \pm s.d. ($n=3$ independent animals). **c**, Haematoxylin and eosin (H&E) staining of heart, kidney, liver, spleen and tumour tissue from PARx-treated and untreated A549 xenografts. Scale bar, 100 μ m. **d**, TUNEL staining of tumour tissue from PARx-treated and untreated A549 xenografts. Brown staining indicates apoptotic cell death. Scale bar, 25 μ m. **e**, Quantification of TUNEL staining. Data are presented as mean values \pm s.d. ($n=6$ biologically independent samples). Statistical analysis was performed using two-tailed Student's *t*-test ($\alpha=0.05$), *** $P<0.001$.

GSH levels. All animals received PARx via retro-orbital injection once every three days for 21 days. Representative images of tumours from group 1 and 2 are shown in Fig. 6c. At the completion of the study, no notable increase in tumour size was observed in group 1, whereas the tumour volume of group 2 had increased to over 1,000 mm³ (Fig. 6d) and the mice had lost substantial body weight (Fig. 6e). It is possible that gemcitabine is intrinsically less effective for U87 tumours. In addition, we cannot rule out a scenario where uptake of PARx in group 1 tumours is greater. However, we can conclude that PARx is not being activated in the U87 tumours owing to a lack of PA signal enhancement in vivo, which is supported by the in vitro and cell-based assays we have previously performed. When the identity of the animals was revealed, we found that we were accurate in each instance, with six of seven mice correctly assigned with greater than 95% confidence.

Evaluation of PACDx in orthotopic lung cancer and liver metastasis models. PA imaging of the lung is an outstanding challenge due to a limited acoustic window through the rib cage and attenuation of the acoustic signal by gas present in air sacs. However, to demonstrate the potential versatility of PACDx, it is essential for us to evaluate its performance in relevant lung cancer models. To this end, we utilized A549 luciferase cells to generate orthotopic lung tumours for PA imaging. Luciferase-expressing cells were used because bioluminescence can be employed to visualize whether the procedure was successful and to subsequently track tumour growth. Before inoculation, we determined that the levels of GSH in wild-type and A549 luciferase cells were indistinguishable (Supplementary

Fig. 27). Six weeks after inoculation, IVIS imaging showed a strong bioluminescent signal in the lung region, indicating successful inoculation (Supplementary Fig. 28). Cross-sectional PA imaging was then performed (Fig. 6f) to reveal a vascularized region where the cancer cells were inoculated (Supplementary Fig. 30). The identity of the tumours was confirmed ex vivo at the conclusion of the study (Supplementary Fig. 31). After initial background scans were acquired, PACDx (or a vehicle control) was administered systemically and final images were recorded after 1 h. All data were processed via spectral unmixing to distinguish the PA signal of PACDx from background due to blood. We observed no change in the PA intensity for the control group ($PA_{\text{Final}}/PA_{\text{Initial}}=0.99\pm 0.16$) (Fig. 6g,h). However, the ratio in the tumour region was 3.17 ± 0.91 , indicating that PACDx had successfully detected elevated GSH in an orthotopic lung cancer model.

Beyond the primary tumour, we also wanted to evaluate PACDx in a liver metastasis model because ~40% of lung tumours have metastasized by the time of diagnosis, with liver being the most common metastatic site⁴⁵. Unfortunately, metastasis was inconsistent using the orthotopic lung cancer model described above. As such, we generated a heterotopic liver cancer model using A549 luciferase cells to test PACDx. When the tumours were imaged via cross-sectional PA imaging, we did not observe any notable changes in the PA intensity for the control group ($PA_{\text{Final}}/PA_{\text{Initial}}=0.94\pm 0.19$), but noted a significant turn-on response in the tumour region ($PA_{\text{Final}}/PA_{\text{Initial}}=3.03\pm 0.97$) (Supplementary Fig. 32a–c). This key experiment further demonstrates the broad utility of PACDx.

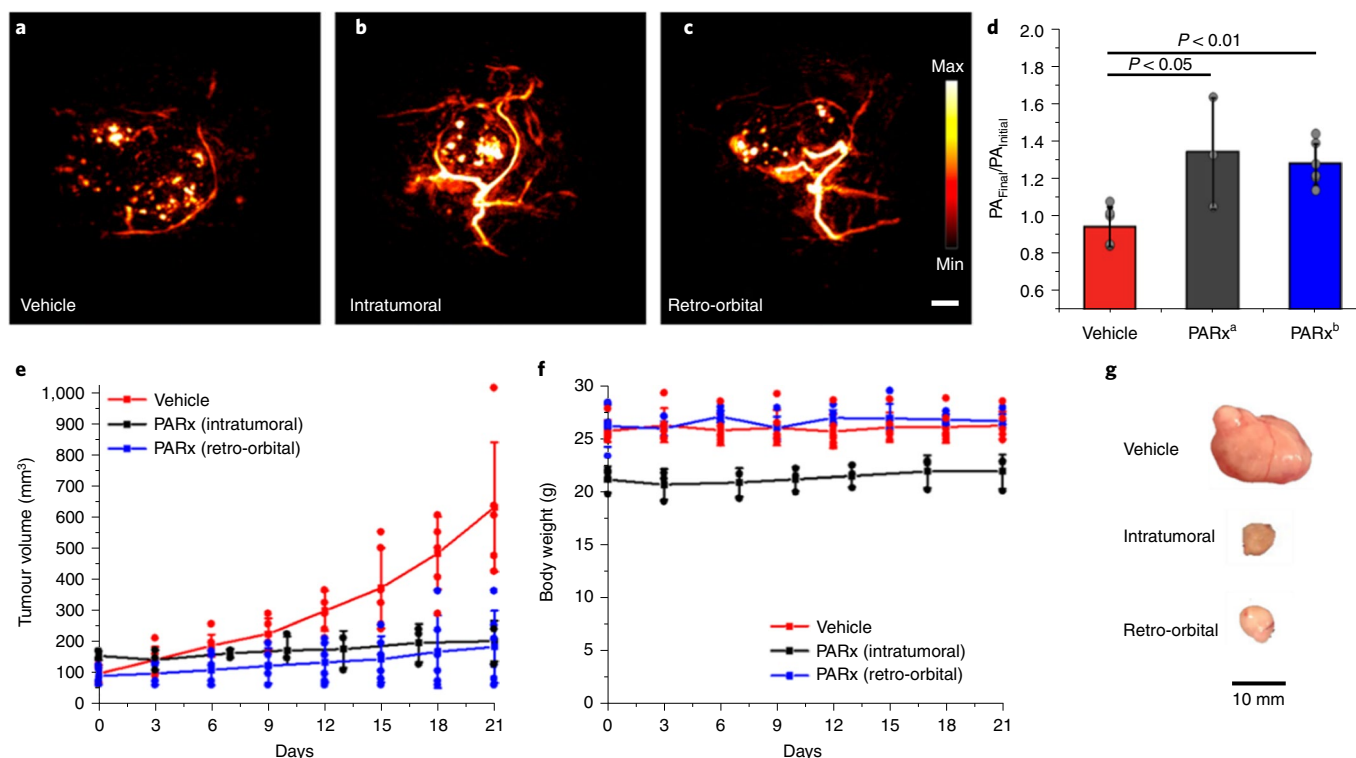


Fig. 5 | Determination of PARx efficacy in a murine model of lung cancer. **a–c**, PA images of tumours after treatment with vehicle (10% DMSO/PBS) (**a**), intratumoral injection of PARx (100 μ M, 10% DMSO/PBS) (**b**) or retro-orbital injection of PARx (400 μ M, 10% DMSO/PBS) (**c**). Samples were irradiated at 680 nm. Scale bar, 2 mm. **d**, PA signal after treatment with vehicle ($n=6$ independent animals) or PARx (^aintratumoral injection, $n=3$ independent animals; ^bretro-orbital injection, $n=6$ independent animals). Data are presented as mean values \pm s.d. (imaging performed when the tumour volume was <200 mm³). **e**, Average tumour volume after treatment with vehicle ($n=6$ independent animals) or intratumoral ($n=3$ independent animals) or retro-orbital injection ($n=6$ independent animals) of PARx over 21 days. **f**, Average body weight after treatment with vehicle or intratumoral or retro-orbital injection of PARx over 21 days. **g**, Representative tumours that were treated with vehicle ($n=6$ independent animals), intratumoral injection of PARx ($n=3$ independent animals) or retro-orbital injection of PARx ($n=6$ independent animals). Statistical analysis was performed using the Kruskal–Wallis test (Bonferroni correction: $\alpha = \alpha/n = 0.05/3 = 0.01667$).

Discussion

The identification of disease biomarkers and the subsequent use of this information to guide therapeutic decision making is highly desirable. In this study, we have utilized a physical organic approach to guide the development of a PA imaging-based CDx for the detection of GSH in murine models of lung cancer. In contrast to commercial probes (for example, GSH Red, $\lambda_{\text{max}} = 580$ nm)⁴⁶, PACDx absorbs maximally in the NIR window, and this property facilitates access to deeper regions of the body. Moreover, it is noteworthy that GSH is typically not considered to be an ideal cancer biomarker because current sensing strategies are too insensitive to distinguish between normal and pathological levels, especially in vivo. For example, 5 μ M GSH is sufficient to fully activate 2.5 μ M GSH Red within 1 h. To overcome this challenge, we performed precision tuning to optimize the S_NAr reactivity, which enabled us to reliably differentiate GSH in the 0.1–10 mM range within the same timeframe. The potential advantage of employing an imaging-based approach rather than a conventional in vitro testing strategy is the potential to visualize changes that occur during disease progression in real time.

We also developed a highly effective prodrug that utilizes the same GSH-mediated activation mechanism to selectively release gemcitabine from a PA imaging dye. Although we could have directly installed the new trigger onto gemcitabine, the ability to perform PA imaging provides us with a powerful handle to monitor drug delivery. Moreover, we did not want to drastically alter the cellular uptake or biodistribution, because the HD dye scaffold has been shown to target tumours, presumably due to the intrinsic

positive charge. We envision further exploiting this robust design to selectively deliver other cancer drugs to tumours. With regards to gemcitabine, it is an FDA-approved drug and one of the first-line treatment options for lung cancer. Unfortunately, it is characterized by rapid metabolism, poor bioavailability and low tumour uptake. As a result, frequent doses must be administered to ensure a therapeutic response, and this can lead to severe liver damage. Because PARx is only activated in lung cancer cells, we were able to demonstrate through different dosing regimens (every 7 days versus every 3 days for 21 days) that PARx did not display any off-target toxicity.

At the onset of this work, our primary objective was to develop a PA imaging-based CDx that could identify subjects with lung cancer based on elevated GSH levels. An additional goal was to employ the CDx to identify patients with cancer who would respond to treatment versus those that would not. We were able to design an unprecedented blind study to evaluate the performance of PACDx in the context of these two aims. Through the application of PACDx, we were able to stratify seven mice bearing different tumour types into two groups. Subsequent treatment with the prodrug demonstrated that the group suspected of having lung cancer did indeed respond. When the identity of each animal was revealed, we were pleased to find that we could accurately distinguish between different cancer types based on PA imaging. This study showcases the potential use of PA imaging to detect critical biomarkers and has allowed us to predict—before treatment—which group of animals will have the greatest therapeutic efficacy when treated with PARx.

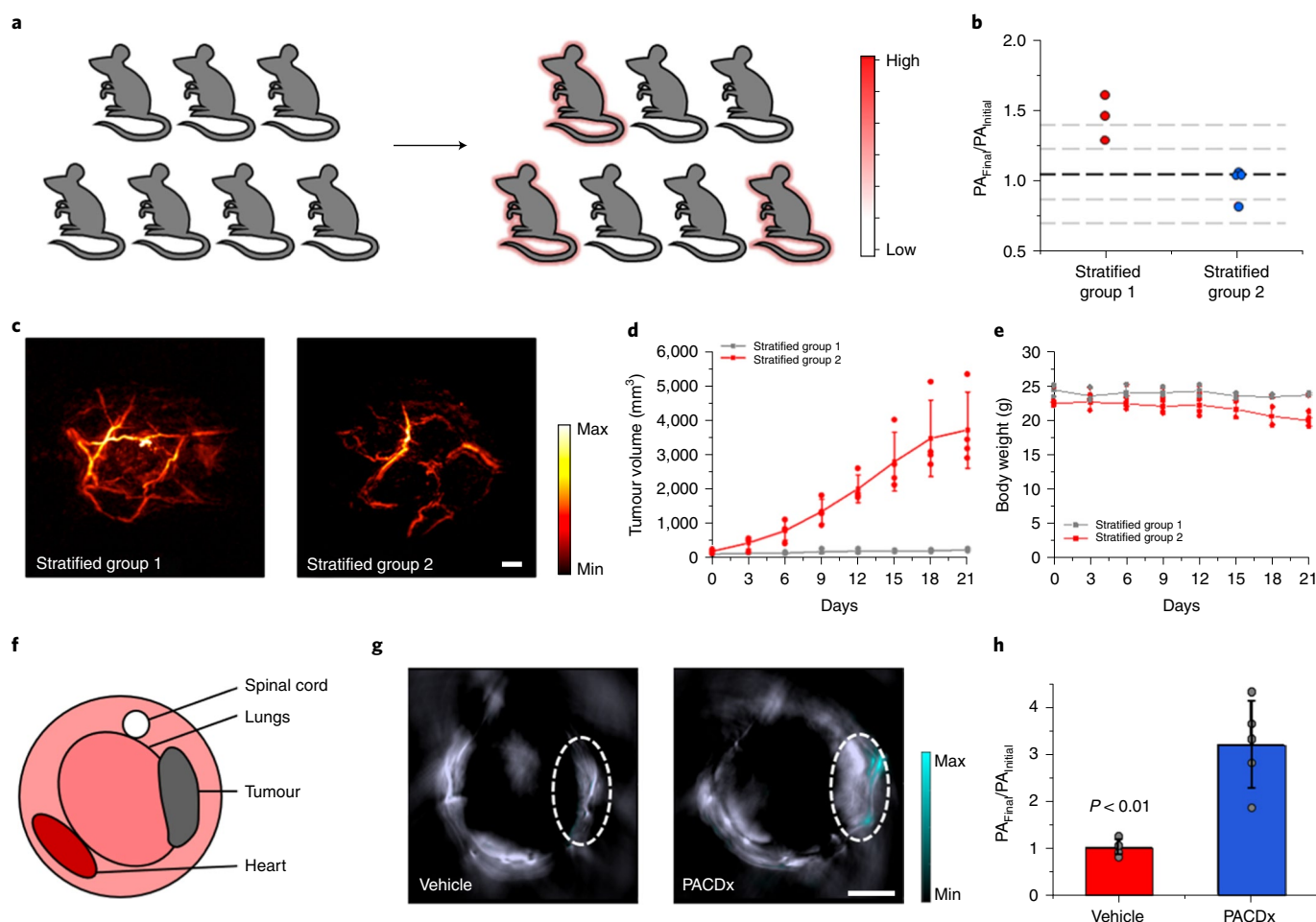


Fig. 6 | Application of PACDx and PARx in unbiased animal studies. **a**, Schematic illustrating the stratification of a patient group based on PA signal intensity in a blind study. **b**, Stratification based on PA fold turn-on after retro-orbital injection of PACDx (400 μ M, 150 μ l, 10% DMSO in saline). The diagnostic threshold was defined as the mean PA fold turn-on after retro-orbital injection of vehicle (150 μ l, 10% DMSO in saline, $n=9$ independent animals) in healthy mice $+2$ s.d. to obtain 95% confidence. The black dashed line indicates the diagnostic threshold and the grey dashed lines indicate s.d. Normalized PA turn-on of stratified groups 1 ($n=3$ independent animals) and 2 ($n=4$ independent animals) are shown. Data are presented as mean values \pm s.d. **c**, Representative PA images of stratified groups 1 ($n=3$ independent animals) and 2 ($n=4$ independent animals) after administration of PACDx. Samples were irradiated at 680 nm. Scale bar, 2 mm. **d,e**, Average tumour volume (**d**) and body weight (**e**) of stratified groups 1 ($n=3$ independent animals) and 2 ($n=4$ independent animals) during a 21-day treatment period with PARx. Data are presented as mean values \pm s.d. **f**, Cross-section schematic of a mouse to reference the positioning of the lungs and tumour. **g**, Representative spectrally unmixed multi-spectral optoacoustic tomography (MSOT) images of the lungs 1 h post-injection of vehicle (150 μ l, 10% DMSO in saline) or PACDx (400 μ M, 150 μ l, 10% DMSO in saline). Scale bar, 5 mm. **h**, Average PA signal from MSOT imaging ($n=5$ independent animals). Statistical analysis was performed using a two-tailed Mann-Whitney U test ($\alpha=0.05$, $P=0.007$).

Owing to the versatile nature of PACDx, we envision that it will find utility in a broad range of important biomedical applications. For example, we have already demonstrated that PACDx can be employed as a fluorogenic probe to detect elevated GSH in live cells using confocal microscopy. Although many fluorescent-based GSH probes exist^{47–50}, we envision that the optimized chemical reactivity and NIR capabilities of PACDx will make it ideal for the detection and tracking of GSH in patient-derived tumour organoids, as well as patient-derived xenografts via optical imaging. The ability to choose between imaging modes (optical versus PA), will present a user with maximal flexibility when designing an experiment. Because PACDx was optimized to discriminate high GSH levels from physiological concentrations, we were able to use it in our study to detect lung cancer. This was demonstrated using PA imaging in multiple animal models of lung cancer, including a subcutaneous xenograft model, an intrahepatic model and an orthotopic lung model. Moreover, beyond targeting lung tumours, we anticipate PACDx and PARx can be employed to detect other conditions and tumour types fea-

turing elevated GSH levels. Finally, we envision that PACDx can be used to aid drug development efforts, because PA imaging can help to confirm and quantify delivery in real time. Beyond preclinical applications, the potential of our new approach in the clinic will be contingent on the availability of instrumentation that facilitates imaging beyond several centimetres. Because PA imaging is a ‘light-in, sound-out’ technique, sufficient light must reach an imaging probe before a signal can be generated. This is one of the major obstacles of translating this technology. However, the development of endoscopic PA set-ups can overcome this challenge, because the region of interest can be illuminated from within the body, bypassing tissue that can attenuate incident light.

Online content

Any methods, additional references, Nature Research reporting summaries, source data, extended data, supplementary information, acknowledgements, peer review information; details of author contributions and competing interests; and statements of

data and code availability are available at <https://doi.org/10.1038/s41557-021-00804-0>.

Received: 27 April 2020; Accepted: 27 August 2021;
Published online: 25 October 2021

References

- Siegel, R. L., Miller, K. D. & Jemal, A. Cancer statistics, 2020. *CA Cancer J. Clin.* **70**, 7–30 (2020).
- Dracopoli, N. C. & Boguski, M. S. The evolution of oncology companion diagnostics from signal transduction to immuno-oncology. *Trends Pharmacol. Sci.* **38**, 41–54 (2017).
- Agarwal, A., Ressler, D. & Snyder, G. The current and future state of companion diagnostics. *Pharmgenomics Pers. Med.* **8**, 99–110 (2015).
- Wang, L. V. & Hu, S. Photoacoustic tomography: in vivo imaging from organelles to organs. *Science* **335**, 1458–1462 (2012).
- Hejblom, M. et al. Photoacoustic image patterns of breast carcinoma and comparisons with magnetic resonance imaging and vascular stained histopathology. *Sci. Rep.* **5**, 11778 (2015).
- Yang, M. et al. Photoacoustic/ultrasound dual imaging of human thyroid cancers: an initial clinical study. *Biomed. Opt. Express* **8**, 3449–3457 (2017).
- Jo, J. et al. A functional study of human inflammatory arthritis using photoacoustic imaging. *Sci. Rep.* **7**, 15026 (2017).
- Liu, Y., Zhang, L., Li, S., Han, X. & Yuan, Z. Imaging molecular signatures for clinical detection of scleroderma in the hand by multispectral photoacoustic elastic tomography. *J. Biophoton.* **11**, e201700267 (2018).
- Reinhardt, C. J. & Chan, J. Development of photoacoustic probes for in vivo molecular imaging. *Biochemistry* **57**, 194–199 (2018).
- Knox, H. J. & Chan, J. Acoustogenic probes: a new frontier in photoacoustic imaging. *Acc. Chem. Res.* **51**, 2897–2905 (2018).
- Li, H., Zhang, P., Smaga, L. P., Hoffman, R. A. & Chan, J. Photoacoustic probes for ratiometric imaging of copper(II). *J. Am. Chem. Soc.* **137**, 15628–15631 (2015).
- Mishra, A., Jiang, Y., Roberts, S., Ntziachristos, V. & Westmeyer, G. G. Near-infrared photoacoustic imaging probe responsive to calcium. *Anal. Chem.* **88**, 10785–10789 (2016).
- Roberts, S. et al. Calcium sensor for photoacoustic imaging. *J. Am. Chem. Soc.* **140**, 2718–2721 (2018).
- Wang, S. et al. Activatable small-molecule photoacoustic probes that cross the blood–brain barrier for visualization of copper(II) in mice with Alzheimer's disease. *Angew. Chem. Int. Ed.* **58**, 12415–12419 (2019).
- Lucero, M. Y. et al. Activity-based photoacoustic probe for biopsy-free assessment of copper in murine models of Wilson's disease and liver metastasis. *Proc. Natl Acad. Sci. USA* **118**, e2106943118 (2021).
- Knox, H. J. et al. A bioreducible N-oxide-based probe for photoacoustic imaging of hypoxia. *Nat. Commun.* **8**, 1794 (2017).
- Knox, H. J., Kim, T. W., Zhu, Z. & Chan, J. Photophysical tuning of N-oxide-based probes enables ratiometric photoacoustic imaging of tumor hypoxia. *ACS Chem. Biol.* **13**, 1838–1843 (2018).
- Chen, M. et al. Simultaneous photoacoustic imaging of intravascular and tissue oxygenation. *Opt. Lett.* **44**, 3773–3776 (2019).
- Zhou, E. Y., Knox, H. J., Liu, C., Zhao, W. & Chan, J. A conformationally restricted aza-BODIPY platform for stimulus-responsive probes with enhanced photoacoustic properties. *J. Am. Chem. Soc.* **141**, 17601–17609 (2019).
- Gardner, S. H. et al. A general approach to convert hemicyanine dyes into highly optimized photoacoustic scaffolds for analyte sensing. *Angew. Chem. Int. Ed.* **60**, 18860–18866 (2021).
- Yin, L. et al. Quantitatively visualizing tumor-related protease activity in vivo using a ratiometric photoacoustic probe. *J. Am. Chem. Soc.* **141**, 3265–3273 (2019).
- Levi, J. et al. Design, synthesis and imaging of an activatable photoacoustic probe. *J. Am. Chem. Soc.* **132**, 11264–11269 (2010).
- Reinhardt, C. J., Zhou, E. Y., Jorgensen, M. D., Partipilo, G. & Chan, J. A ratiometric acoustogenic probe for in vivo imaging of endogenous nitric oxide. *J. Am. Chem. Soc.* **140**, 1011–1018 (2018).
- Reinhardt, C. J., Xu, R. & Chan, J. Nitric oxide imaging in cancer enabled by steric relaxation of a photoacoustic probe platform. *Chem. Sci.* **11**, 1587–1592 (2020).
- Lucero, M. Y. et al. Development of NIR-II photoacoustic probes tailored for deep-tissue sensing of nitric oxide. *J. Am. Chem. Soc.* **143**, 7196–7202 (2021).
- Chen, Z. et al. An optical/photoacoustic dual-modality probe: ratiometric in/ex vivo imaging for stimulated H2S upregulation in mice. *J. Am. Chem. Soc.* **141**, 17973–17977 (2019).
- Forman, H. J., Zhang, H. & Rinna, A. Glutathione: overview of its protective roles, measurement and biosynthesis. *Mol. Aspects Med.* **30**, 1–12 (2009).
- Balendiran, G. K., Dabur, R. & Fraser, D. The role of glutathione in cancer. *Cell Biochem. Funct.* **22**, 343–352 (2004).
- Gamcsik, M. P., Kasibhatla, M. S., Teeter, S. D. & Colvin, O. M. Glutathione levels in human tumors. *Biomarkers* **17**, 671–691 (2012).
- Russo, A., DeGraff, W., Friedman, N. & Mitchell, J. B. Selective modulation of glutathione levels in human normal versus tumor cells and subsequent differential response to chemotherapy drugs. *Cancer Res.* **46**, 2845–2848 (1986).
- Giustarini, D. et al. Glutathione, glutathione disulfide and S-glutathionylated proteins in cell cultures. *Free Radical Biol. Med.* **89**, 972–981 (2015).
- Estrela, J. M., Ortega, A. & Obrador, E. Glutathione in cancer biology and therapy. *Crit. Rev. Clin. Lab. Sci.* **43**, 143–181 (2006).
- Zhang, J. et al. Synthesis and characterization of a series of highly fluorogenic substrates for glutathione transferases, a general strategy. *J. Am. Chem. Soc.* **133**, 14109–14119 (2011).
- Shibata, A. et al. Fluorogenic probes using 4-substituted-2-nitrobenzenesulfonyl derivatives as caging groups for the analysis of human glutathione transferase catalyzed reactions. *Analyst* **138**, 7326–7330 (2013).
- Lee, M. H. et al. Disulfide-cleavage-triggered chemosensors and their biological applications. *Chem. Rev.* **113**, 5071–5109 (2013).
- Maeda, H. et al. 2,4-Dinitrobenzenesulfonyl fluoresceins as fluorescent alternatives to Ellman's reagent in thiol-quantification enzyme assays. *Angew. Chem. Int. Ed.* **44**, 2922–2925 (2005).
- Hansch, C., Leo, A. & Taft, R. W. A survey of Hammett substituent constants and resonance and field parameters. *Chem. Rev.* **91**, 165–195 (1991).
- van Iersel, M. L. P. S. et al. Inhibition of glutathione S-transferase activity in human melanoma cells by α,β -unsaturated carbonyl derivatives. Effects of acrolein, cinnamaldehyde, citral, crotonaldehyde, curcumin, ethacrynic acid and trans-2-hexenal. *Chem. Biol. Interact.* **102**, 117–132 (1996).
- Rahman, I., Kode, A. & Biswas, S. K. Assay for quantitative determination of glutathione and glutathione disulfide levels using enzymatic recycling method. *Nat. Protoc.* **1**, 3159–3165 (2006).
- Manegold, C. Gemcitabine (Gemzar) in non-small cell lung cancer. *Expert Rev. Anticancer Therapy* **4**, 345–360 (2004).
- Hayashi, H., Kurata, T. & Nakagawa, K. Gemcitabine: efficacy in the treatment of advanced stage nonsquamous non-small cell lung cancer. *Clin. Med. Insights Oncol.* **5**, 177–184 (2011).
- Toschi, L., Finocchiaro, G., Bartolini, S., Gioia, V. & Cappuzzo, F. Role of gemcitabine in cancer therapy. *Future Oncol.* **1**, 7–17 (2005).
- He, M., Xuehong, C. & Yepeng, L. Small molecular gemcitabine prodrugs for cancer therapy. *Curr. Med. Chem.* **26**, 5562–5582 (2019).
- Ullman-Cullere, M. H. & Foltz, C. J. Body condition scoring: a rapid and accurate method for assessing health status in mice. *Lab. Anim. Sci.* **49**, 319–323 (1999).
- Milovanovic, I. S., Stjepanovic, M. & Mitrovic, D. Distribution patterns of the metastases of the lung carcinoma in relation to histological type of the primary tumor: an autopsy study. *Ann. Thorac. Med.* **12**, 191–198 (2017).
- Glutathione (GSH) Probes* (Ursa Bioscience, 2013); <https://ursabioscience.com/technology/gsh-probes>
- Jiang, X. et al. Quantitative real-time imaging of glutathione. *Nat. Commun.* **8**, 16087 (2017).
- Zhou, H. et al. Intracellular endogenous glutathione detection and imaging by a simple and sensitive spectroscopic off-on probe. *Analyst* **143**, 2390–2396 (2018).
- Guo, R. et al. GSH activated biotin-tagged near-infrared probe for efficient cancer imaging. *Theranostics* **9**, 3515–3525 (2019).
- Zou, Y. et al. Bioimaging of glutathione with a two-photon fluorescent probe and its potential application for surgery guide in laryngeal cancer. *ACS Sens.* **5**, 242–249 (2020).

Publisher's note Springer Nature remains neutral with regard to jurisdictional claims in published maps and institutional affiliations.

© The Author(s), under exclusive licence to Springer Nature Limited 2021

Reporting Summary. Further information on research design is available in the Nature Research Reporting Summary linked to this Article.

Data availability

All data are available within the Article and its Supplementary Information. Alternatively, data are available upon request from the corresponding author.

Acknowledgements

This work was supported by the National Institutes of Health (R35GM133581). M.Y.L. acknowledges the Alfred P. Sloan Foundation for financial support. Major funding for the 500-MHz Bruker CryoProbe™ was provided by the Roy J. Carver Charitable Trust (Muscatine, Iowa; grant no. 15-4521) to the School of Chemical Sciences NMR Lab. The Q-TOF Ultima mass spectrometer was purchased in part with a grant from the National Science Foundation, Division of Biological Infrastructure (DBI-0100085). We also acknowledge the Core Facilities at the Carl R. Woese Institute for Genomic Biology for access to the Zeiss LSM 700 confocal microscope and corresponding software. We also acknowledge I. Dobrucka and the Molecular Imaging Laboratory at the Beckman Institute for use of the IVIS imaging system. M.Y.L. thanks H. Knox for initial animal training and assistance with the NanoZoomer. We thank T. Bearrood and C. Anorma for assistance with initial confocal imaging experiments, L. Akin for aid with mass spectrometry experiments, S. Anakk and A. Dean for help with interpreting results from H&E staining experiments, N. Herndon and J. Xu for help with generating the

orthotopic lung cancer and liver metastasis models, S. Gardner for providing 4T1 tumour models, J. Sarol and A. Kaur from Biostatistics, Epidemiology, & Research Design at the Interdisciplinary Health Sciences Institute (UIUC) for aid in statistical analysis, and A. Bennet for helpful discussions.

Author contributions

M.Y.L. performed all experiments in this study that include chemical synthesis, in vitro characterization, cellular studies, tumour model studies, in vivo imaging and sample preparation for ex vivo analysis. J.C. assisted with the blinded animal study. M.Y.L. and J.C. analysed the data and prepared the manuscript. J.C. conceived the project, with intellectual contributions from M.Y.L.

Competing interests

The authors declare no competing interests.

Additional information

Supplementary information The online version contains supplementary material available at <https://doi.org/10.1038/s41557-021-00804-0>.

Correspondence and requests for materials should be addressed to Jefferson Chan.

Peer review information *Nature Chemistry* thanks Junjie Yao, Deju Ye and the other, anonymous, reviewer(s) for their contribution to the peer review of this work.

Reprints and permissions information is available at www.nature.com/reprints.

Reporting Summary

Nature Research wishes to improve the reproducibility of the work that we publish. This form provides structure for consistency and transparency in reporting. For further information on Nature Research policies, see our [Editorial Policies](#) and the [Editorial Policy Checklist](#).

Statistics

For all statistical analyses, confirm that the following items are present in the figure legend, table legend, main text, or Methods section.

- | | |
|-------------------------------------|---|
| n/a | Confirmed |
| <input type="checkbox"/> | <input checked="" type="checkbox"/> The exact sample size (n) for each experimental group/condition, given as a discrete number and unit of measurement |
| <input type="checkbox"/> | <input checked="" type="checkbox"/> A statement on whether measurements were taken from distinct samples or whether the same sample was measured repeatedly |
| <input type="checkbox"/> | <input checked="" type="checkbox"/> The statistical test(s) used AND whether they are one- or two-sided
<i>Only common tests should be described solely by name; describe more complex techniques in the Methods section.</i> |
| <input checked="" type="checkbox"/> | <input type="checkbox"/> A description of all covariates tested |
| <input type="checkbox"/> | <input checked="" type="checkbox"/> A description of any assumptions or corrections, such as tests of normality and adjustment for multiple comparisons |
| <input checked="" type="checkbox"/> | <input type="checkbox"/> A full description of the statistical parameters including central tendency (e.g. means) or other basic estimates (e.g. regression coefficient) AND variation (e.g. standard deviation) or associated estimates of uncertainty (e.g. confidence intervals) |
| <input type="checkbox"/> | <input checked="" type="checkbox"/> For null hypothesis testing, the test statistic (e.g. F , t , r) with confidence intervals, effect sizes, degrees of freedom and P value noted
<i>Give P values as exact values whenever suitable.</i> |
| <input checked="" type="checkbox"/> | <input type="checkbox"/> For Bayesian analysis, information on the choice of priors and Markov chain Monte Carlo settings |
| <input checked="" type="checkbox"/> | <input type="checkbox"/> For hierarchical and complex designs, identification of the appropriate level for tests and full reporting of outcomes |
| <input checked="" type="checkbox"/> | <input type="checkbox"/> Estimates of effect sizes (e.g. Cohen's d , Pearson's r), indicating how they were calculated |

Our web collection on [statistics for biologists](#) contains articles on many of the points above.

Software and code

Policy information about [availability of computer code](#)

Data collection

Data analysis

For manuscripts utilizing custom algorithms or software that are central to the research but not yet described in published literature, software must be made available to editors and reviewers. We strongly encourage code deposition in a community repository (e.g. GitHub). See the Nature Research [guidelines for submitting code & software](#) for further information.

Data

Policy information about [availability of data](#)

All manuscripts must include a [data availability statement](#). This statement should provide the following information, where applicable:

- Accession codes, unique identifiers, or web links for publicly available datasets
- A list of figures that have associated raw data
- A description of any restrictions on data availability

Field-specific reporting

Please select the one below that is the best fit for your research. If you are not sure, read the appropriate sections before making your selection.

- Life sciences Behavioural & social sciences Ecological, evolutionary & environmental sciences

For a reference copy of the document with all sections, see [nature.com/documents/nr-reporting-summary-flat.pdf](https://www.nature.com/documents/nr-reporting-summary-flat.pdf)

Life sciences study design

All studies must disclose on these points even when the disclosure is negative.

Sample size	<input type="text" value="The sample sizes in the paper were estimated from the conventional rules in previous publications."/>
Data exclusions	<input type="text" value="No data were excluded from the analysis."/>
Replication	<input type="text" value="All attempts at replication were successful."/>
Randomization	<input type="text" value="All mice were randomly divided into different groups."/>
Blinding	<input type="text" value="The investigators who collected and analyzed the data were blinded to group allocation."/>

Reporting for specific materials, systems and methods

We require information from authors about some types of materials, experimental systems and methods used in many studies. Here, indicate whether each material, system or method listed is relevant to your study. If you are not sure if a list item applies to your research, read the appropriate section before selecting a response.

Materials & experimental systems

n/a	Included in the study
<input checked="" type="checkbox"/>	<input type="checkbox"/> Antibodies
<input type="checkbox"/>	<input checked="" type="checkbox"/> Eukaryotic cell lines
<input checked="" type="checkbox"/>	<input type="checkbox"/> Palaeontology and archaeology
<input type="checkbox"/>	<input checked="" type="checkbox"/> Animals and other organisms
<input checked="" type="checkbox"/>	<input type="checkbox"/> Human research participants
<input checked="" type="checkbox"/>	<input type="checkbox"/> Clinical data
<input checked="" type="checkbox"/>	<input type="checkbox"/> Dual use research of concern

Methods

n/a	Included in the study
<input checked="" type="checkbox"/>	<input type="checkbox"/> ChIP-seq
<input checked="" type="checkbox"/>	<input type="checkbox"/> Flow cytometry
<input checked="" type="checkbox"/>	<input type="checkbox"/> MRI-based neuroimaging

Eukaryotic cell lines

Policy information about [cell lines](#)

Cell line source(s)	<input type="text" value="All cells were obtained from the American Type Culture Collection."/>
Authentication	<input type="text" value="All cell lines were authenticated in the American Type Culture Collection and used as received."/>
Mycoplasma contamination	<input type="text" value="All cells tested negative for mycoplasma contamination."/>
Commonly misidentified lines (See ICLAC register)	<input type="text" value="No misidentified lines were used in the study."/>

Animals and other organisms

Policy information about [studies involving animals](#); [ARRIVE guidelines](#) recommended for reporting animal research

Laboratory animals	<input type="text" value="Nu/J athymic nude female mice, 1-3 months"/>
Wild animals	<input type="text" value="The study did not involve wild animals"/>
Field-collected samples	<input type="text" value="The study did not involve samples collected from the field"/>
Ethics oversight	<input type="text" value="Institutional Animal Care and Use Committee"/>

Note that full information on the approval of the study protocol must also be provided in the manuscript.